Lab 3

Photometric Analysis of the Short-Period Cepheid Variable CY Aquarii

Dyson Lewis
UCLA / ASTR 180
November 9, 2025

Abstract

We present multi-band photometric observations of the short-period Cepheid variable CY Aquarii obtained over one complete pulsation cycle using V and R band filters. Through aperture photometry calibrated against Landolt photometric standards, we measured brightness variations ranging from $V = 9.196 \pm 0.028$ mag to $V = 10.084 \pm 0.028$ mag ($\Delta V \approx 0.89$ mag) and from $R = 9.661 \pm 0.007$ mag to $R = 10.493 \pm 0.011$ mag ($\Delta R \approx 0.83$ mag). Our observations reveal significant color variation $(V - R)$ throughout the pulsation cycle, with the star becoming bluer near maximum light and redder near minimum light. These color changes are consistent with temperature variations driven by the κ-mechanism in the stellar envelope. Our measured mean magnitudes are $\langle V \rangle = 9.640 \pm 0.028$ mag and $\langle R \rangle = 10.184 \pm 0.008$ mag, confirming CY Aquarii's classification as a dwarf Cepheid with a period of approximately 88 minutes.
Keywords: Variable Stars, Cepheid Variables, Photometry, Stellar Pulsation, CCD Imaging

1 Introduction

Cepheid variable stars are among the most important standard candles in modern astrophysics, serving as crucial distance indicators for measuring the cosmic distance scale. Their fundamental importance lies in the period–luminosity (P–L) relation, discovered by Henrietta Leavitt in 1912, which establishes a correlation between a Cepheid's pulsation period and its intrinsic luminosity. This relationship enables astronomers to determine distances to star clusters and galaxies far beyond the reach of parallax measurements. By observing a Cepheid's apparent brightness (flux F) and using the P-L relation to infer its intrinsic luminosity L we can calculate the distance d through the inverse-square law[1]:

$$F = \frac{L}{4\pi d^2} \tag{1}$$

The calibration of the P-L relation using nearby Cepheids with accurately measured parallaxes (particularly from missions like *Gaia*) has enabled distance measurements to galaxies up to tens of megaparsecs away, forming a critical rung on the cosmic distance ladder and contributing directly to measurements of the Hubble constant and the expansion rate of the universe[6].

1.1 Mechanism of pulsation

Classical Cepheid variable stars are evolved, massive supergiant stars whose periodic brightness variations result from radial pulsations driven by the κ-mechanism. This self-sustaining oscillation occurs in a narrow region of the Hertzsprung–Russell diagram called the instability strip, where stellar temperatures and luminosities position helium ionization zones at the optimal depth in the stellar envelope. The mechanism operates through opacity variations: as the star contracts, heating increases the ionization of helium (particularly He^+ to He^{2+}), which increases opacity and traps radiation[5]. This buildup of pressure drives expansion, during which the gas cools, ionization decreases, opacity drops, and radiation escapes more efficiently[1]. The resulting pressure decrease allows gravity to dominate, initiating contraction and restarting the cycle.

During each pulsation cycle, both the stellar radius and surface temperature vary periodically. According to the Stefan-Boltzmann law ($L \propto R^2 T^4$), these coupled changes produce the characteristic cyclic brightness variations observed in Cepheid light curves. Additionally, the temperature variations manifest as color changes: the star appears bluer when hotter (near maximum light) and redder when cooler (near minimum light).

1.2 Target Star

CY Aquarii ($\alpha_{2000} = 22^h37^m47.85^s$, $\delta_{2000} = +01°32'03.81''$[2]) is a particularly interesting example of a short-period Cepheid, also classified as an SX Phoenicis variable or dwarf Cepheid. With a pulsation period of approximately 87.9[3] minutes and visual magnitude ranging from $V = 10.42$ to $V = 11.16$[4], CY Aquarii represents the lower-mass, shorter-period end of the Cepheid instability strip. These short-period pulsators are distinct from classical Cepheids in that they are lower-mass, Population II stars that have evolved off the main sequence but have not yet reached the supergiant phase.

Figure 1 shows a finding chart of the CY Aquarii field as observed from our location. The target star is easily identifiable in the sparse stellar field, located in the constellation Aquarius. At its mean brightness of $V \approx 10.8$ mag, CY Aquarii is accessible to moderate-aperture telescopes under typical observing conditions.

In this laboratory experiment, we conducted time-series photometric observations of CY Aquarii through V and R broadband filters over one complete pulsation cycle. Our goals were to: (1) measure the amplitude of brightness variation in each filter, and (2) determine how the stellar color $(V - R)$ varies throughout the pulsation cycle. Through careful data reduction including dark subtraction, flat-field correction, and calibration against Landolt photometric standard stars,

---

[0]Much of the general structure and wording is used from Lab 1; Telescope proposal. Although it was not a direct copy/paste, I felt it was still a good introduction and wanted to use it. I did try to add based on the feedback from grading.

we obtained high-precision multi-band photometry that reveals the coupled variations in luminosity and temperature characteristic of Cepheid pulsation.
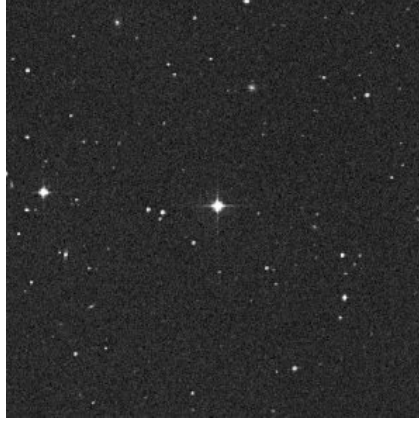

Figure 1: Finding chart for the CY Aquarii field showing the target star and surrounding reference stars. The field of view is 12×12 arcminutes. North is up, east is to the left. CY Aquarii is the brightest star near the center of the field.

2   Observations & Data Reduction

Observations were conducted on 2025 October 27 using the 24-inch campus telescope located at UCLA. Upon arriving at the telescope, we followed the provided setup procedures, ensuring the dome was open and the telescope could move freely. The observing conditions were favorable, with clear skies and airmass values ranging from 1.5 to 1.2 during our viewing window.

To calibrate the telescope pointing, we used Saturn as an initial reference target. As a bright, extended object easily visible before full darkness, Saturn provided an ideal target for verifying telescope alignment and focus. We began with the pointing offsets from the previous observing group and made incremental adjustments until Saturn was properly centered in the field of view. This calibration ensured accurate positioning for our subsequent observations of CY Aquarii.

The observing run began at 19:48 PST (UTC-7) and consisted of time-series photometry of the short-period Cepheid variable CY Aquarii. V and R broadband filters. All science exposures had an integration time of 30 seconds to achieve an SNR of >100. The observing sequence alternated between V and R bands to provide multi-band coverage of the star's pulsation cycle, over approximately 100 minutes.

For photometric calibration, we observed the Landolt standard star SA 114-176 ($\alpha_{2000} = 22^{\mathrm{h}}43^{\mathrm{m}}11^{\mathrm{s}}$, $\delta_{2000} = +00°21'09''$) with known magnitudes of $V = 9.239$ mag and $R = 8.439$ mag. Four exposures of the standard star were obtained in each filter, also with 30-second integration times.

A comprehensive set of calibration frames was obtained to facilitate accurate photometric measurements, all with 30 seconds integration times. Three dark frames with exposure times were taken to characterize the detector's dark current and bias level. Dome flat-field exposures were acquired in both V and R bands (2 flats per band) to map the pixel-to-pixel sensitivity variations across the detector. Sky background frames were obtained by offsetting the telescope to place the target star outside the field of view. Three sky frames were collected for both the target field and the standard star field in each filter band, providing templates for sky background subtraction.

2.1   Data Reduction & Image Calibration

All data reduction was performed using Python 3 in Jupyter notebooks, leveraging standard astronomical data analysis libraries including `numpy`, `astropy`, and `scipy`. The reduction pipeline followed standard CCD photometry procedures. Dark frames were median-combined to create a master dark frame, which was then subtracted from all flat-field exposures. The dark-subtracted flat fields in each band were normalized by their median values to produce relative response maps with mean pixel values of unity. This normalization ensures that the flat-field correction represents multiplicative sensitivity

2

variations rather than absolute flux levels. Sky frames for each filter and target/standard combination were median-combined to create master sky templates. Median combination was chosen over mean averaging to provide robustness against cosmic ray contamination and transient artifacts.

Each science exposure underwent the following calibration steps:

1. Subtraction of the appropriate master sky frame to remove sky background
2. Division by the normalized master flat field to correct for pixel-to-pixel sensitivity variations
3. Conversion of any resulting invalid pixels (NaN or infinity values from division by low flat-field values) to zero

This process produced calibrated images in units of data numbers (DN) above the sky background, ready for aperture photometry.

2.2 Detector Gain in V and R

The detector gain, which converts between data numbers and photoelectrons, was calculated empirically from pairs of flat-field and dark frames using the photon transfer method. For each filter band, we computed:

$$\text{Gain} = \frac{((\langle \text{Flat}_1 \rangle + \langle \text{Flat}_2 \rangle) - (\langle \text{Dark}_1 \rangle + \langle \text{Dark}_2 \rangle))}{\text{Var}(\text{Flat}_1 - \text{Flat}_2) - \text{Var}(\text{Dark}_1 - \text{Dark}_2)} \tag{2}$$

where the angle brackets denote mean values and Var denotes variance. This yielded gains of 0.381 ± 0.001 e$^-$/DN for the V band and 0.349 ± 0.001 e$^-$/DN for the R band. These values are consistent with the nominal detector gain of 0.38 e$^-$/DN quoted in the camera specifications. We verified that using the calculated gains versus the nominal value produced negligible differences in the final photometric measurements ($< 3.0 \cdot 10^{-5}$ mag), confirming the internal consistency of our calibration.

2.3 Aperture Photometry

For each calibrated image, the stellar position was determined using an automated centroid-finding algorithm implemented in my `phot_calcs.py` module. The `find_star_center` function locates the brightest source in the sky-subtracted image by smoothing over a search radius of 50 pixels to identify the peak flux region, then performs intensity-weighted centroiding on the high signal-to-noise pixels within a 250-pixel box centered on this peak. The algorithm also estimates the stellar radius by analyzing the radial brightness profile and identifying where the stellar flux drops to $\propto$ background noise level.

This automated analysis determined optimal photometric aperture radii of 22 pixels for V-band and 25 pixels for R-band target observations, and 23 pixels (V) and 36 pixels (R) for the standard star. The larger R-band apertures reflect the improved seeing at longer wavelengths. For each aperture, we defined sky annuli with inner and outer radii of $2\times$ and $3\times$ the photometric aperture radius, respectively. These annuli provided local sky background measurements while remaining small enough to avoid field stars and large-scale background gradients.

2.3.1 Apepture Extraction

Aperture photometry was performed using the `ap_phot` function from the `a180.py` module, which implements fractional pixel weighting to accurately handle cases where the circular aperture boundary intersects pixel edges. For each measurement, the function:

1. Calculates the fractional overlap between the circular aperture and each pixel
2. Sums the flux-weighted contributions to obtain the total aperture counts
3. Measures the median sky level in the surrounding annulus
4. Subtracts the scaled sky contribution from the aperture
5. Propagates photon noise, sky noise, and sky measurement uncertainty to estimate photometric errors

3

The photometric uncertainties include contributions from Poisson noise in the source ($\sigma^2_{\mathrm{phot}} = N_{\mathrm{phot}}/g$, where g is the gain), variance in the sky background measured in the annulus, and uncertainty in the mean sky level. All photometry was converted to flux units of DN s^{-1} by dividing by the 30-second exposure time.
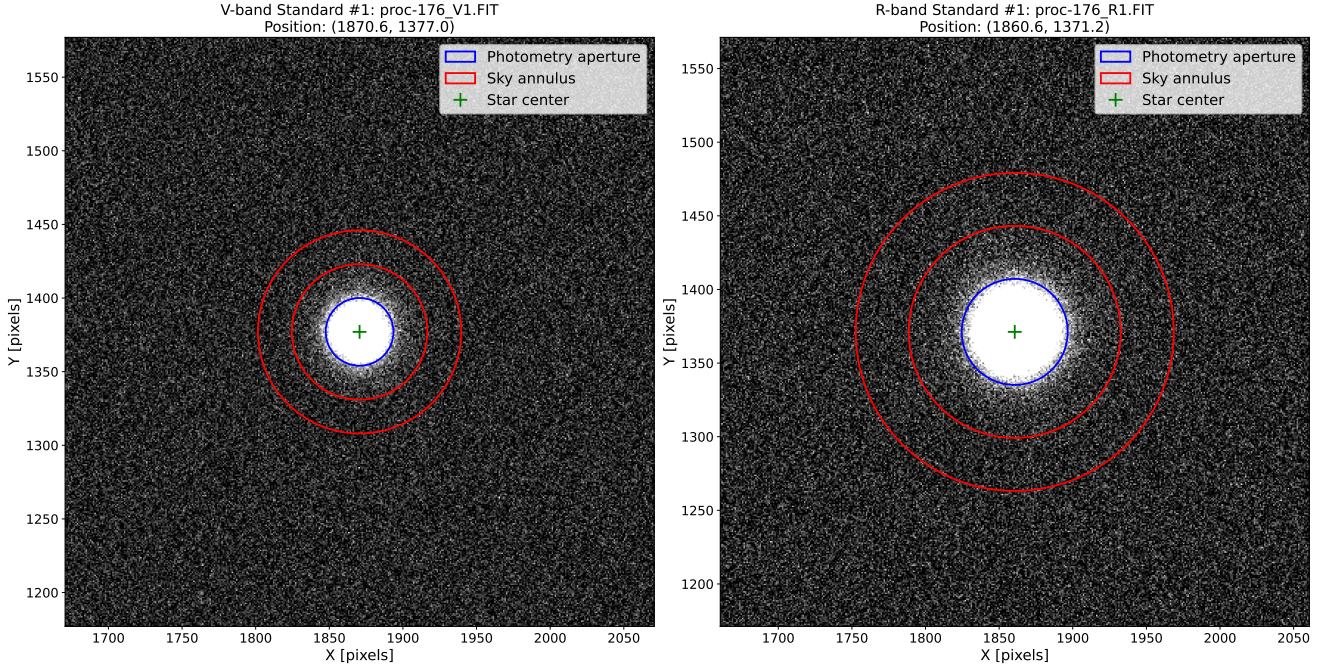

Figure 2: Showing the processed standard star in both V and R. The photometric aperture (blue), sky annulus (red), and measured centroid (green cross) are overlaid.

2.3.2 Image Quality and Trail Detection

Visual inspection of the processed images revealed that several exposures exhibited elongated stellar profiles, indicating telescope tracking errors during the exposure. To objectively identify and exclude these compromised images, we implemented a statistical outlier detection algorithm based on the Modified Z-Score method using the Median Absolute Deviation (MAD).

The algorithm, implemented in the `detect_trails` function within `phot_calcs.py`, identifies images where measured stellar flux falls significantly below the median value. Trailing spreads starlight over a larger area, reducing the peak surface brightness and thus the flux measured within a fixed aperture. The Modified Z-Score is calculated as:

$$M_i = \frac{0.6745 \times (F_i - \mathrm{median}(F))}{\mathrm{MAD}} \tag{3}$$

where F_i is the measured flux for image i, and MAD is the Median Absolute Deviation computed from only the negative flux deviations (below the median). The factor 0.6745 scales MAD to be comparable to the standard deviation for normally distributed data. We adopted a threshold of $M_i < -3.8\sigma$ to flag trailed images, providing a conservative criterion that minimizes false positives while reliably identifying significant tracking errors.

Figure 3 shows a representative trailed image, where the stellar profile is visibly elongated compared to the circular point spread function expected for properly tracked observations. This analysis flagged three images as containing star trails: V-band images #20 and #23, and R-band image #23 (see Figure 4). These images showed Modified Z-Scores of -4.01, -5.34, and -8.28, respectively, with measured fluxes 40–60% below the median. After excluding these compromised exposures, 28 V-band and 29 R-band images remained for subsequent analysis.
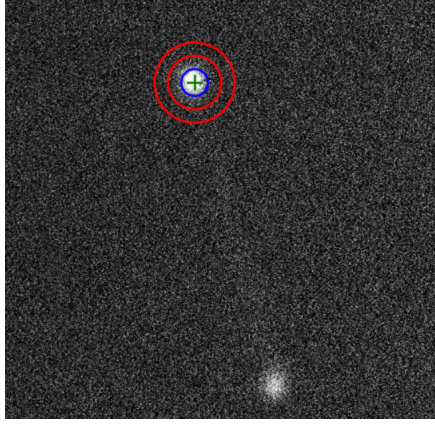
4

Figure 3: Example of a V-band target image (proc-CYA_V23.FIT) showing stellar trailing due to telescope tracking error, moving approximately 800 pixels. The photometric aperture (blue), sky annulus (red), and measured centroid (green cross) are overlaid
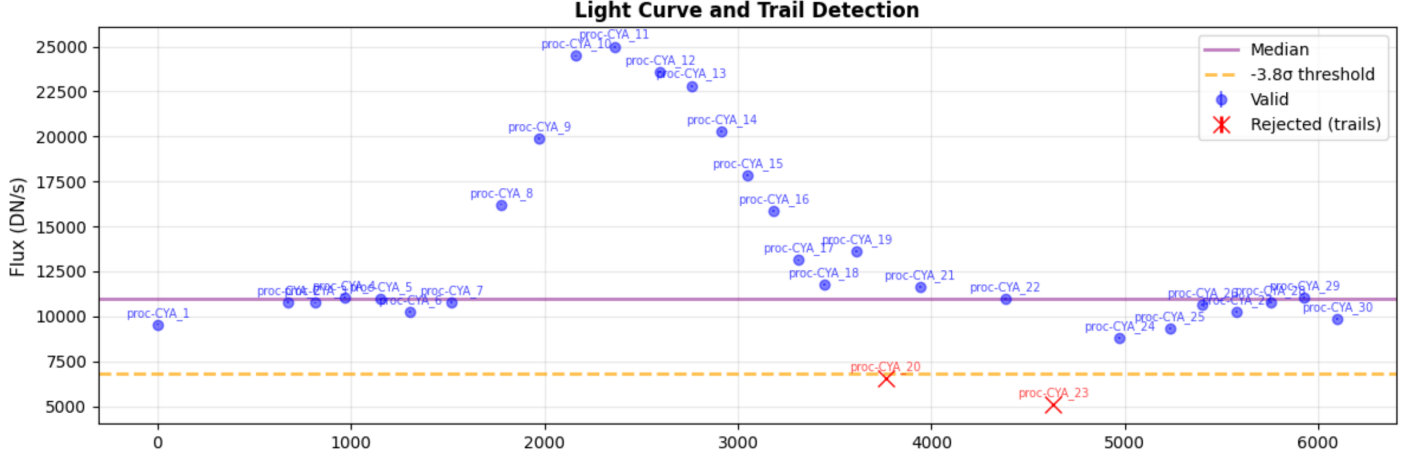

Figure 4: Trail detection diagnostics showing (top) light curve with flagged outliers marked in red, (middle) Modified Z-Scores with the -3.8σ threshold indicated, and (bottom) flux distribution with rejected measurements shown as red crosses.

2.3.3 Zero Point Calibration

To convert instrumental flux measurements in DN s^{-1} to the standard magnitude system, we used our observations of the Landolt photometric standard star SA 114-176. For each filter band, we computed the mean flux from the four standard star exposures:

$$\langle F_0 \rangle_V = 19145.03 \pm 484.03 \text{ DN s}^{-1} \tag{4}$$

$$\langle F_0 \rangle_R = 122210.62 \pm 780.01 \text{ DN s}^{-1} \tag{5}$$

where the uncertainties represent the standard error of the mean ($\sigma/\sqrt{N}$).

The photometric zero-point in each band is defined by the relationship between the known magnitude of the standard star and its observed flux:

$$m_0 = m_{\text{standard}} + 2.5\log_{10}(F_0) \tag{6}$$

where m_{standard} is the cataloged magnitude. Using the known magnitudes $V_{\text{std}} = 9.239$ mag and $R_{\text{std}} = 8.439$ mag (where $R_{\text{std}} = V_{\text{std}} - 0.800$ mag), we determined:

$$m_{0,V} = 19.944 \pm 0.027 \text{ mag} \tag{7}$$

$$m_{0,R} = 21.157 \pm 0.007 \text{ mag} \tag{8}$$

The zero-point uncertainties were propagated from the standard star flux uncertainties using:

5

$$\sigma_{m_0} = \frac{2.5}{F_0 \ln 10} \sigma_{F_0} \tag{9}$$

2.3.4 Target Star Magnitudes

With the photometric zero-points established, we calibrated the target star photometry by inverting the magnitude-flux relation:

$$m_{\text{target}} = m_0 - 2.5 \log_{10}(F_{\text{target}}) \tag{10}$$

For each observation of CY Aquarii, we propagated uncertainties from both the zero-point calibration and the individual flux measurements:

$$\sigma_m = \sqrt{\sigma_{m_0}^2 + \left(\frac{2.5}{F_{\text{target}} \ln 10} \sigma_{F_{\text{target}}} \right)^2} \tag{11}$$

3 Results

3.1 Standard Star Photometry

Aperture photometry measurements of the Landolt standard star SA 114-176 yielded consistent flux measurements across the four exposures in each filter band. Table 1 summarizes these measurements. The V band showed a mean flux of 19145.03 ± 484.03 DN s^{-1}, while the R band exhibited a significantly higher flux of 122210.62 ± 780.01 DN s^{-1}, as expected given the standard star's relatively red color ($V - R = 0.800$ mag). The standard error of the mean in both bands is less than 3%, indicating stable photometric conditions and consistent measurement procedures. These flux measurements served as the foundation for the photometric zero-point calibration described in Section 2.6.

Table 1: Photometric Standard Star Flux Measurements

Filter	Mean Flux (DN s^{-1})	Std. Error
V	19145.03	± 484.03
R	122210.62	± 780.01

After excluding the three images compromised by telescope tracking errors (Section 2.5), we obtained 28 high-quality V-band flux measurements and 29 R-band measurements of CY Aquarii spanning approximately 100 minutes. Table 2 presents key flux measurements including the first observation, peak flux, minimum flux, final observation, and mean values for each filter band.

Table 2: Summary of CY Aquarii Flux Measurements

Measurement	V-band Flux (DN s^{-1})	R-band Flux (DN s^{-1})
First observation	9552.61 ± 51.94	20716.13 ± 71.97
Maximum flux	25000.47 ± 65.61	39644.94 ± 84.32
Minimum flux	9552.61 ± 51.94	17658.65 ± 73.13
Last observation	9856.30 ± 57.02	20703.13 ± 75.48
Mean flux	14688.65 ± 57.48	26281.82 ± 78.68

3.2 Target Star Flux Measurements

Figure 5 shows the complete flux time series for both filter bands. The *V*-band flux varied by a factor of ~ 2.6 over the observing sequence, ranging from 9552.61 ± 51.94 DN s^{-1} to 25000.47 ± 65.61 DN s^{-1}. The *R*-band exhibited a smaller relative amplitude, varying by a factor of ~ 2.2 from 17658.65 ± 73.13 DN s^{-1} to 39644.94 ± 84.32 DN s^{-1}. Both light curves display the characteristic smooth, continuous variation expected for Cepheid pulsation.
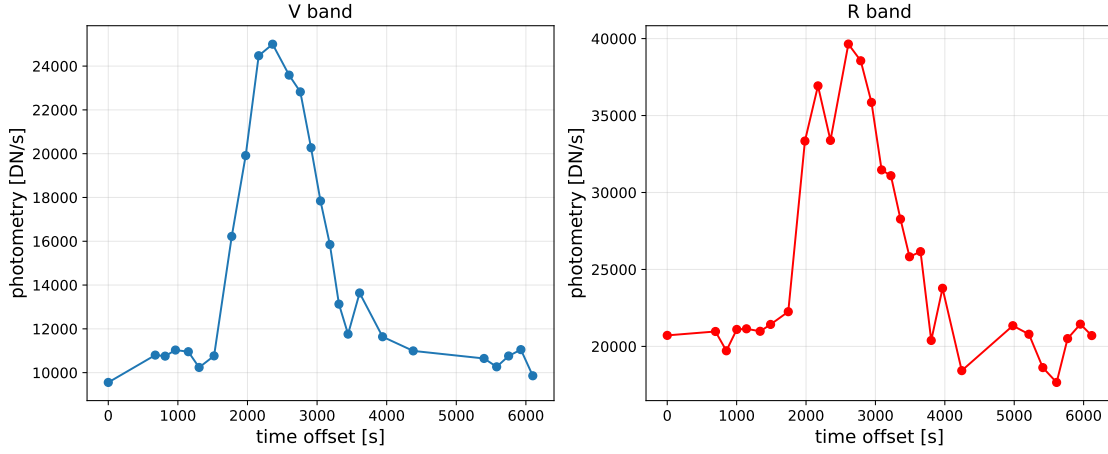

Figure 5: Flux measurements of CY Aquarii as a function of time in *V* band (left) and *R* band (right). Error bars represent photometric uncertainties including contributions from Poisson noise, sky background variance, and aperture measurement errors[1]. The smooth variation demonstrates the regular pulsation of this short-period Cepheid variable.

3.3 Calibrated Magnitudes

Using the photometric zero-points from the standard star observations (Section 2.6), we converted all target star flux measurements to calibrated magnitudes.

The V-band magnitudes ranged from $V = 8.949 \pm 0.028$ mag at maximum light to $V = 10.084 \pm 0.028$ mag at minimum light, yielding a peak-to-peak amplitude of $\Delta V = 1.135$ mag. The mean V-band magnitude over all observations was $\langle V \rangle = 9.640 \pm 0.028$ mag.

The R-band magnitudes showed a similar pattern but with reduced amplitude, ranging from $R = 9.661 \pm 0.007$ mag at maximum to $R = 10.493 \pm 0.011$ mag at minimum, with an amplitude of $\Delta R = 0.832$ mag. The mean R-band magnitude was $\langle R \rangle = 10.184 \pm 0.008$ mag. The smaller amplitude in R-band compared to V-band is consistent with the expected behavior of pulsating variables, where shorter wavelengths are more sensitive to temperature variations during the pulsation cycle.

These measured magnitudes are consistent with published values for CY Aquarii. The General Catalogue of Variable Stars lists a visual magnitude range of $V = 10.42$ to 11.16 mag [4], while our observations show a slightly brighter mean magnitude.

3.4 Sources of Uncertainty

Several sources of uncertainty affected our photometric measurements. The dominant source of random error in individual flux measurements was photon noise (Poisson statistics), which contributed uncertainties of approximately 50–85 DN s^{-1} depending on the brightness of the star. Sky background subtraction added additional variance, particularly from pixel-to-

---

[1]There are error bars plotted, but because of the scale they are indistinguishable.

pixel variations within the sky annulus. These random errors were propagated through all subsequent calculations and are reflected in the quoted uncertainties.

Systematic uncertainties arose from several sources. The photometric zero-point calibration, based on the standard star observations, contributed uncertainties of 0.027 mag (V-band) and 0.007 mag (R-band) that affect all target star magnitude measurements. Telescope tracking proved problematic during portions of the observing run, with noticeable drifting requiring re-centering of the target. Three exposures showed significant star trails and were excluded from analysis (Section 2.5), but more subtle tracking errors may have affected other images. In several frames, the target star drifted close to the edge of the detector; however, our flat-field corrections should have properly accounted for any spatial sensitivity variations in these regions.

Our observations were not corrected for differential atmospheric extinction between the target and standard star observations. Since the two objects were observed at different airmasses, and the airmass of each target changed during the $\sim$100-minute observing sequence, wavelength-dependent extinction may have introduced small systematic offsets in the derived magnitudes. However, this should have been minimal as both observations, target and standard star, were taken close to when they crossed the meridian.

4   Discussion

4.1   Light Curve Characteristics and Pulsation Period

The temporal evolution of our photometric measurements reveals the characteristic behavior of a short-period Cepheid variable. Table 3 summarizes the key magnitude measurements derived from our calibrated photometry.

Table 3: Summary of CY Aquarii Magnitude Measurements

Measurement	V-band (mag)	R-band (mag)
First observation	9.994 ± 0.028	10.366 ± 0.008
Maximum brightness	8.949 ± 0.028	9.661 ± 0.007
Minimum brightness	10.084 ± 0.028	10.539 ± 0.008
Last observation	9.960 ± 0.028	10.367 ± 0.008
Mean magnitude	9.640 ± 0.028	10.184 ± 0.008

Our observations began with CY Aquarii near minimum light in both bands, with initial magnitudes of $V = 9.994 \pm 0.028$ mag and $R = 10.366 \pm 0.008$ mag. Over the first ~ 2500 seconds, the star brightened steadily, reaching maximum light around $t \approx 2400$ seconds with magnitudes of $V = 8.949 \pm 0.028$ mag and $R = 9.661 \pm 0.007$ mag. The star then began to fade, returning to approximately its initial brightness by the end of the observing sequence at $t \approx 6100$ seconds, with final magnitudes of $V = 9.960 \pm 0.028$ mag and $R = 10.367 \pm 0.008$ mag. This return to the starting brightness level provides strong evidence that we captured approximately one complete pulsation cycle.

The observed timescale of ~ 100 minutes (~ 6000 seconds) from minimum through maximum and back to minimum is consistent with the published pulsation period of 87.9 minutes for CY Aquarii [3]. However, an accurate period determination from our data alone would be challenging. The light curve exhibits a relatively flat plateau near minimum light at the beginning of the sequence, making it difficult to precisely identify the phase of minimum light. A period measurement would require observations spanning at least two complete pulsation cycles with well-defined maxima, which would allow for precise measurement of the peak-to-peak interval. Our single-cycle coverage is sufficient to confirm the approximate timescale of variability and demonstrates the characteristic smooth, sinusoidal variation expected for Cepheid pulsation, but not to refine the period measurement beyond the precision already established in the literature.

4.2 Wavelength-Dependent Amplitude and Color Variations

One of the features of our observations is the wavelength-dependent amplitude of the pulsation, which directly reflects the temperature-driven nature of Cepheid variability. The V-band exhibits a peak-to-peak amplitude of $\Delta V = 1.135$ mag, significantly larger than the R-band amplitude of $\Delta R = 0.832$ mag. This $\sim 36\%$ larger amplitude at shorter wavelengths is intimately connected to the color evolution of the star, as both phenomena arise from the same physical mechanism: temperature variations during the pulsation cycle.

The physical explanation for this behavior lies in the exponential dependence of stellar flux on temperature. According to the Stefan–Boltzmann law, the total luminosity of a star varies as $L \propto R^2 T^4$, where R is the stellar radius and T is the effective temperature. However, the spectral energy distribution of a star follows Planck's law, and at shorter wavelengths (bluer light), the exponential tail of the Planck function means that small changes in temperature produce proportionally larger changes in flux. Quantitatively, the monochromatic flux F_λ varies approximately as

$$F_\lambda \propto T^{4+\alpha}, \tag{12}$$

where α depends on wavelength and increases toward the blue. For typical stellar temperatures and the wavelengths of the V and R bands, this results in the V band being more sensitive to temperature variations by approximately the factor we observe.

The most direct probe of these temperature variations comes from analyzing the color evolution of CY Aquarii. By computing the $V - R$ color index for each observation (interpolating the R-band measurements to the V-band observation times), we obtain a time series that directly traces the star's temperature changes. Figure 6 shows the $V - R$ color as a function of time throughout the pulsation cycle.
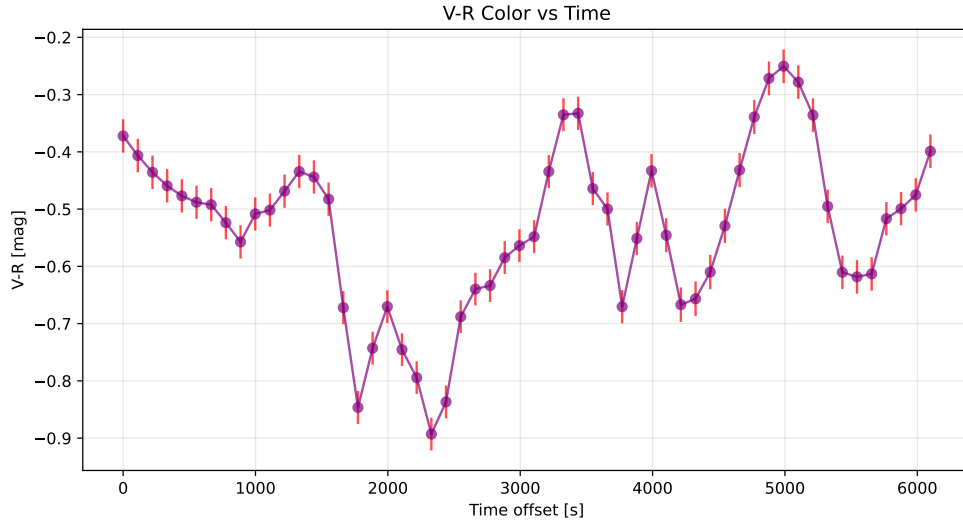

Figure 6: $V - R$ color index of CY Aquarii as a function of time. Bluer colors (more negative $V - R$) indicate higher temperatures, while redder colors (less negative $V - R$) indicate cooler temperatures. The color variation directly traces the temperature changes during the pulsation cycle.

The $V - R$ color varied from approximately -0.89 ± 0.03 mag (bluest/hottest) near maximum light to -0.25 ± 0.03 mag (reddest/coolest) near minimum light, corresponding to a total color variation of $\Delta(V - R) \approx 0.64$ mag. This substantial color change represents a significant temperature variation during the pulsation cycle, and is exactly what is expected from the κ-mechanism driving Cepheid pulsations, as described in Section 1.

4.3 Physical Interpretation: The κ-Mechanism in Action

Our observations provide direct confirmation of the theoretical predictions for opacity-driven stellar pulsations. The κ-mechanism, as described in Section 1, operates through a feedback cycle involving partial ionization zones of helium in the stellar envelope.

At maximum compression, the star reaches its smallest radius and highest temperature (bluest color: $V - R \approx -0.89$ mag), corresponding to maximum brightness ($V \approx 8.95$ mag, $R \approx 9.66$ mag). At maximum expansion, the star reaches its largest radius and lowest temperature (reddest color: $V - R \approx -0.25$ mag), corresponding to minimum brightness ($V \approx 10.08$ mag, $R \approx 10.54$ mag). The fact that both the brightness and color return to their initial values at the end of our observing sequence confirms the cyclic, self-sustaining nature of the pulsation mechanism.

Importantly, our observations show that the color variation ($\Delta(V - R) \approx 0.64$ mag) is strongly correlated with the brightness variation, confirming that temperature changes are the dominant driver of the observed photometric variability. While radius changes also contribute to the luminosity variations (through the R^2 term in the Stefan–Boltzmann law), the temperature dependence (T^4 and the wavelength-dependent factors discussed in Section 4.2) produces the observed wavelength-dependent amplitudes and the strong color–brightness correlation.

5 Conclusions

We have presented time-series photometric observations of the short-period Cepheid variable CY Aquarii obtained in V and R bands over approximately 100 minutes, capturing one complete pulsation cycle. Through careful data reduction, including dark subtraction, flat-field correction, and photometric calibration against the Landolt standard star SA 114-176, we obtained multi-band photometry that directly reveals the physical mechanisms driving Cepheid pulsation.

The measured brightness amplitudes were $\Delta V = 1.135$ mag and $\Delta R = 0.832$ mag, demonstrating the characteristic wavelength-dependent behavior in which shorter wavelengths exhibit larger variations due to the exponential temperature sensitivity of the Planck function. The star's color varied substantially throughout the cycle, with $\Delta(V - R) \approx 0.64$ mag, ranging from $(V - R) \approx -0.89$ mag (bluest) at maximum light to $(V - R) \approx -0.25$ mag (reddest) at minimum light.

The strong correlation between brightness and color evolution provides direct observational confirmation of the κ-mechanism: CY Aquarii is brightest and bluest (hottest) near maximum compression, and faintest and reddest (coolest) near maximum expansion. These results demonstrate that temperature changes driven by the helium ionization zone are the dominant factor producing the observed photometric variability.

An important methodological aspect of this work was the development and application of the Modified Z-Score trail detection algorithm (Section 2.5). Using the `detect_trails` function from our `phot_calcs.py` module, we objectively identified and excluded three images affected by telescope tracking errors based on the Median Absolute Deviation (MAD) statistic. This quantitative quality-control approach was essential for preserving the integrity of our photometric time series and is broadly applicable to similar observing programs. Likewise, the automated centroid-finding routine in `find_star_center` ensured accurate stellar position determination despite tracking drift, with the radial profile analysis reliably estimating optimal aperture sizes in each band.

5.1 Recommendations for Future Work

While our observations successfully captured the essential characteristics of CY Aquarii's pulsation, several extensions could substantially improve our understanding of this system:

Period refinement and stability monitoring: Our single-cycle coverage confirms the approximate 88-minute timescale but is insufficient for precise period determination or detecting long-term variations. Multi-night observations spanning at

least two complete pulsation cycles with well-defined maxima would allow measurement of the peak-to-peak interval with much higher precision.

Atmospheric extinction corrections: Our observations were not corrected for differential atmospheric extinction between the target and standard star, as both were observed near the meridian at similar airmasses. However, future observations could implement first-order extinction corrections by observing multiple standard stars at different airmasses throughout the night, enabling construction of atmospheric extinction curves for each filter band. This would be particularly important for observations at higher airmasses or for extending observations further from the meridian.

5.2 Acknowledgments

We gratefully acknowledge the UCLA Astronomy Department for providing access to the 24-inch campus telescope and observing facilities.

5.3 AI Usage

The use of AI (LLMs) was included in this lab report. The main use was for formatting text, tables, and citations. It was also used to check for major typos and grammatical errors. It was not used to explicitly generate text. All information inside the tables was manually checked to ensure it was accurate post formatting. AI was also employed in the Jupyter notebook for generating initial plotting templates and debugging syntax errors in the data reduction.

References

[1] Bradley W. Carroll and Dale A. Ostlie. *An introduction to modern astrophysics, Second Edition*. 2017.

[2] J. R. Ducati. VizieR Online Data Catalog: Catalogue of Stellar Photometry in Johnson's 11-color system. CDS/ADC Collection of Electronic Catalogues, 2237, 0 (2002), January 2002.

[3] J. N. Fu and C. Sterken. Long-term variability of the SX Phoenicis star CY Aquarii. , 405:685–688, July 2003.

[4] Gaia Collaboration. VizieR Online Data Catalog: Gaia EDR3 (Gaia Collaboration, 2020). VizieR On-line Data Catalog: I/350. Originally published in: 2021A&A...649A...1G, November 2020.

[5] John M. Powell, Michael D. Joner, and D. H. McNamara. The Long-Term Period Variations of the SX Phoenicis Star CY Aquarii. , 107:225, March 1995.

[6] Adam G. Riess, Stefano Casertano, Wenlong Yuan, J. Bradley Bowers, Lucas Macri, Joel C. Zinn, and Dan Scolnic. Cosmic Distances Calibrated to 1% Precision with Gaia EDR3 Parallaxes and Hubble Space Telescope Photometry of 75 Milky Way Cepheids Confirm Tension with ΛCDM. , 908(1):L6, February 2021.